ACS APPLIED MATERIALS & INTERFACES

www.acsami.org

Research Article

Compositional Engineering Study of Lead-Free Hybrid Perovskites for Solar Cell Applications

Roshan Ali,* Zhen-Gang Zhu,* Qing-Bo Yan, Qing-Rong Zheng, Gang Su,* Amel Laref, Chaudry Sajed Saraj, and Chunlei Guo*

Cite This: *ACS Appl. Mater. Interfaces* 2020, 12, 49636−49647

Read Online

ACCESS | Metrics & More | Article Recommendations | Supporting Information

ABSTRACT: Hybrid organic−inorganic perovskite solar cells (HOIPs), especially $CH_3NH_3PbI_3$ ($MAPbI_3$), have received tremendous attention due to their excellent power conversion efficiency (25.2%). However, two fundamental hurdles, long-term stability and lead (Pb) toxicity, prevent HOIPs from practical applications in the solar industry. To overcome these issues, compositional engineering has been used to modify cations at A- and B-sites and anions at the X-site in the general form ABX_3. In this work, we used the density functional theory (DFT) to incorporate Rb, Cs, and FA at the A-site to minimize the volatile nature of MA, while the highly stable Ca^{2+} and Sr^{2+} were mixed with the less stable Ge^{2+} and Sn^{2+} at the B-site to obtain a Pb-free perovskite. To further enhance the stability, we mixed the X-site anions (I/Br). Through this approach, we introduced 20 new perovskite species to the lead-free perovskite family and 7 to the lead-containing perovskite family. The molecular dynamic (MD) simulations, enthalpy formation, and tolerance and octahedral factor study confirm that all of the perovskite alloys we introduced here are as stable as pristine $MAPbI_3$. All Pb-free perovskites have suitable and direct band gaps (1.42−1.77 eV) at the Γ-point, which are highly desirable for solar cell applications. Most of our Pb-free perovskites have smaller effective masses and exciton binding energies. Finally, we show that the introduced perovskites have high absorption coefficients (10^5 cm^{-1}) and strong absorption efficiencies (above 90%) in a wide spectral range (300−1200 nm), reinforcing their significant potential applications. This study provides a new way of searching for stable lead-free perovskites for sustainable and green energy applications.

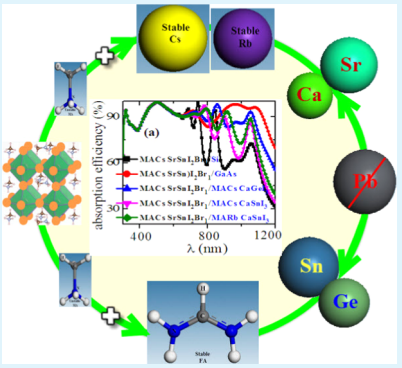

KEYWORDS: *DFT, lead-free hybrid perovskites, optical properties, absorption efficiencies, single-junction solar cells, tandem solar cells*

I. INTRODUCTION

Perovskites with the structure ABX_3 (where A= Rb^+, Cs^+, $CH_3NH_3^+$ (methylammonium, MA), $HC(NH_2)_2^+$ (formamidinium, FA), B= divalent ion (Pb^{2+}, Sn^{2+}, Ge^{2+}, etc.), and X = I^-, Br^-, Cl^-) have recently gained tremendous interest in the field of photovoltaic technology due to their remarkable single-junction power conversion efficiency (PCE = 25.2%).[1] The PCE of perovskite (25.2%) is comparable to the established solar cell PCEs of Si (26.1%) and GaAs (27.8%). $MAPbI_3$ has excellent properties such as a suitable solar absorbing band gap (1.55 eV), sharp optical band edge, high absorption coefficient (10^4−10^5 cm^{-1}), and reduced exciton binding energy (10−30 meV). Long diffusion lengths, high mobility (low effective masses), high defect tolerance, and low fabrication cost (solution-processable at low temperature)[2−11] also make perovskites prominent. Furthermore, perovskites also find uses in the field of lasers, light-emitting diodes (LEDs), photodiodes, and photodetectors.[12−15]

Despite these impressive properties, stability and toxicity are two main concerns in their pathways to the commercialization of these materials. Toxicity happens due to the presence of lead (Pb) at the B-site of $MAPbI_3$. The instability issue arises from the highly volatile nature of the A-site MA cation, which makes it less stable by interacting with the atmosphere (moisture and air), heat, and light. Moreover, orientation of the MA cation is also responsible for the stability of the perovskite phase. $MAPbI_3$ decomposes into CH_3NH_3I, which further degrades into CH_3I and NH_3 at around 80 °C.[16] Hence, the MA cation also poses a key risk in their pathways for commercialization. To overcome the issue of stability, different strategies have been used, including mixing the MA cation with more stable organic/inorganic cations to decrease the highly volatile nature of MA or mix the X-site halide ions. It is noted that the highest efficiency (>20%) solar cells achieved so far consist of complex A-site cation mixing, such as double mixing (MA/FA, Cs/FA, Rb/FA),[17−20] triple mixing (Cs/MA/FA, Rb/MA/FA, Rb/Cs/FA), and tetra mixing (Rb/Cs/MA/FA)[20,21] with better stability. More importantly, the FA cation is present in all of these highly performed mixed perovskites because the FA

Received: August 13, 2020
Accepted: October 6, 2020
Published: October 20, 2020

cation is more thermally stable as compared to MA, also having a red-shifted ideal band gap.[18,22] $FAPbI_3$ was confirmed to be free from phase transition between 25 and 150 °C.[23] However, the FA cation is larger in size as compared to the MA cation, which creates distortion in the lattice and results in a yellow phase (photoinactive) at room temperature. Meanwhile, a black phase (photoactive) could only be achieved at very high temperatures.[18] Somehow, to overcome the issue of the yellow phase, researchers mixed the halide anions (I/Br), and it was noted that mostly the high-PCE perovskites contain 20% of bromide (Br) mixing.[20,21,24,25] On the other hand, on replacing or mixing I with Br, the band gap tuned largely (E_g = 1.55 eV for $MAPbI_3$ and 2.3 eV for $MAPbBr_3$), a blue penalty, which in turn decreases the absorption efficiency.[26,27] Hence, a smaller ratio of Br should be used. In contrast, mixing the A-site cations has a very small impact (decrease) on the band gap because of its weak interaction with the octahedral metal-halide cage.[26]

To obtain stable perovskites, researchers have studied MA-free perovskite materials with PCE < 20% at high temperatures.[20,28,29] Recently, S.-H. Turren-Cruz et al. performed a thin-film study on MA cations and MA-free cations and discovered that MA-free cation-based perovskites are highly stable as compared to the MA-cation-based perovskites and achieved PCE 20.35% for $Rb_5Cs_{10}FAPbI_3$ (highest PCE in MA-free perovskites so far). According to their findings, the thin-film structure cannot provide full evidence for completely avoiding the MA cation in all future perovskites for long-term stability.[30] Researchers are highly interested in a small ratio of Rb incorporation at the A-site due to the smaller ionic radius of Rb.[31] The Rb incorporation not only increases the solar cells' PCE but is also suitable for photodetectors and light-emitting diodes (LEDs).[31] Recently, Rb containing HOIP ($Rb_{0.05}MA_{0.95}PbI_3$) achieved a stable efficiency of 18.8%.[31] It has been investigated that Cs incorporation reduces the number and depth of trap states in perovskite crystals.[30]

For the stability of the perovskite phase, we should first follow Goldschmidt's tolerance factor rules[32] (refer to Section IV). $MAPbI_3$ in highly symmetrical tetragonal (at room temperature) and cubic (at 60 °C) phases is more stable and efficient than that in the less symmetric orthorhombic phase (162 K).[33] The structural phase transitions basically degrade the PCE performance and the stability of the material, which is directly related to Goldschmidt's tolerance factor.[32] In light of the above discussion, to increase the stability and maintain the absorption efficiency, we propose to mix the MA cation with suitable organic or inorganic ions.[34] Furthermore, mixing the halide anions (especially I/Br, Br < 20%) increases the stability with less decrease in PCE.[35] It has also been investigated that mixing divalent species at the B-site of $MAPbI_3$ can also enhance the stability of these hybrid perovskites with strong absorption.[27,36−38]

The second aim of this study is to find out nontoxic suitable alternatives to lead (Pb), having a good absorption efficiency. As Pb is a highly toxic element, its presence on a commercial basis with less stability could be highly dangerous for living organisms because $MAPbI_3$ degrades to PbI_2 in the presence of moisture. Besides this, after the end of lifetime, the solar panel should be sunk properly otherwise it will pollute the environment. Although the solar cell made by Pb-based perovskites can be encapsulated, it is highly desirable to design Pb-free materials from the very beginning. Researchers have an obligation to avoid pollution arising from so-called advanced technology. Therefore, it is necessary to discover environmentally friendly stable hybrid perovskite materials with high absorption for the commercialization of perovskite solar cells. For this purpose, we are introducing some new materials to the perovskite family and expecting their remarkable applications in the PV industry.

In our previously predicted monoreplacement Pb-free study, the group II and XIV elements were investigated with the best alternatives in their 3D counterpart. In single-element replacements, Sn and Ge were the best alternatives to Pb,[27,39,40] which are experimentally synthesized with a lower efficiency (<10%) and a smaller band gap (1.30 eV). However, Sn has a higher mobility (10^2−10^3 cm^2 V^{-1} s^{-1}) as compared to Pb-based perovskites (10−10^2 cm^2 V^{-1} s^{-1}).[41] Basically, the decrease of PCE in MA $(Sn,Ge)I_3$ is due to the oxidation from $(Sn,Ge)^{2+}$ to $(Sn,Ge)^{4+}$. The rapid oxidation of Sn^{2+} to Sn^{4+} makes $MASnI_3$-based perovskites less attractive, while $FASnI_3$ was found stable enough.[42,43] Mixed Sn/Pb perovskites achieved the highest PCE > 19% with mixed Br incorporation.[44] To get desirable band gaps and stable less toxic or nontoxic perovskites, a trend of mixing Pb with other homovalent species or Pb-free mixing is of high interest.[27,37,45,46] After being mixed with Pb, almost all suitable homovalent species (Co, Cu, Fe, Mg, Mn, Ni, Sn, Sr, Zn) were found to have excellent absorption efficiency (Co/Pb = 17.2%, Sn/Pb = 17.6%), tolerance, and stability.[36,47] Through a density functional theory (DFT) study, it was found that mixing Ge/Pb or replacing Pb by mixing Bi/(S,Se) and Bi/(Tl,In) will lead to good absorption and stability.[48−50] Mixing Sr^{2+} with Pb^{2+} ($CsPb_{0.98}Sr_{0.02}I_2Br$, $MA(Pb/Sr)I_3$) also resulted in long carrier lifetimes, excellent V_{oc}, and high fill-factor (85%) with a stable efficiency of 10.8%.[51,52]

It is also to be noted that high-entropy alloys of solids enhance stability, which allows them to be easily synthesized, processed, analyzed, and utilized for different applications.[53] There have been a number of Pb-free perovskite studies for 3D-$MAPbI_3$ with no better optical absorption and stability as discussed in details. According to the above discussion, Sn and Ge are the best alternatives to Pb because of their stability in humid air and high temperature. We hope that PCE will also increase if we mix Sn and Ge with highly stable Ca and Sr ((Ca,Sr)/(Sn,Ge); 12.5/87.5%). Therefore, to solve the issues of stability and toxicity, we are introducing three site mixings (ABX_3) using DFT calculations. By mixing A-site cations (MA/(Cs,Rb,FA); 62.5/37.5%), B-site cations/Pb-free ((Ca,Sr)/(Sn,Ge); 12.5/87.5%), and pure as well as mixed X-site anions (I/Br; 2:1), we aim to obtain highly stable lead-free perovskite materials with excellent absorption efficiency. Using this approach, we expect excellent absorption efficiency and stability.

II. METHODOLOGY

All calculations were performed using the density functional theory (DFT) as implemented in the VASP simulation package.[54] Initially, the Perdew−Burke−Ernzerhof (PBE)[55] functional was used as an exchange correlation functional for structural and electronic calculations, while for accurate band structure calculations, the Heyd−Scuseria−Ernzerhof (HSE06)[56] functional was used. A 2 × 2 × 2 supercell of the tetragonal structure was allowed to relax. The cutoff energy for basis functions was selected to be 520 eV. *K*-points, 3 × 3 × 3, were used for structural relaxation with a force criterion of 0.025 eV $Å^{-1}$. For self-consistency and optical properties, k-

https://dx.doi.org/10.1021/acsami.0c14595
ACS Appl. Mater. Interfaces 2020, 12, 49636−49647

points of 4 × 4 × 4 were used. Special k-points, (0,0,0), (1/2,1/2,1/2), (0,1/2,1/2), and (1/2,0,1/2), were used for band structure calculations. We performed the optical properties with the PBE functional, and then, for corrected optical properties, we applied the scissors operator.

Through *ab initio* calculations, we obtained the real and imaginary parts of the dielectric function and then used them as input files in the COMSOL Multi-physics simulation package for calculating the device absorption efficiencies for all of our predicted perovskite materials. Further details about the method are given in Section I, methodology (Supporting Information).

We performed molecular dynamic (MD) simulations of the 2 × 2 × 2 supercell to confirm the stability of these new materials. For MD simulation, we used PWmat software;[57] the Langevin thermostat was used by fixing the temperature at 300 K. We used the PBE functional while using the norm-conserving pseudopotential (VWR) and the ultrasoft pseudopotential (USPP) from the repository of PWmat. Time steps of 1fs were used due to the large number of light H-atoms in the crystal structures. The total simulation time of 7 ps was used in our calculations.

III. RESULTS AND DISCUSSION

To obtain stable and efficient Pb-free perovskite materials for sustainable and green energy applications, we mixed A-site cations (MA/Rb, MA/Cs, MA/FA; ratio 62.5/37.5%), B-site cations (Ca/(Ge,Sn), Sr/(Ge,Sn); ratio 12.5/87.5%), and X-site halide anions (I/Br; ratio 66.66/33.33%) in the tetragonal crystal structure of $MAPbI_3$, as shown in Figure 1. Calcium (Ca^{2+}) and strontium (Sr^{2+}) have highly stable oxidation states, are environmentally friendly, and are easily available. On the other hand, simply introducing Sn^{2+} and Ge^{2+} at the B-site (Pb) can easily oxidize to Sn^{4+} and Ge^{4+}. Therefore, we mixed highly stable divalent Ca^{2+} and Sr^{2+} to Sn^{2+} and Ge^{2+} to get stable lead-free perovskite materials. We expect that the interaction of stable Ca^{2+} and Sr^{2+} with Ge^{2+} and Sn^{2+} will overcome the issue of their oxidation because doping strengthens the bonding.[53] After successful relaxation of all of the Pb-free perovskite materials, the lattice parameter values with very less variations (<2%) are given in the Supporting Information (Table.S1) with full descriptions.

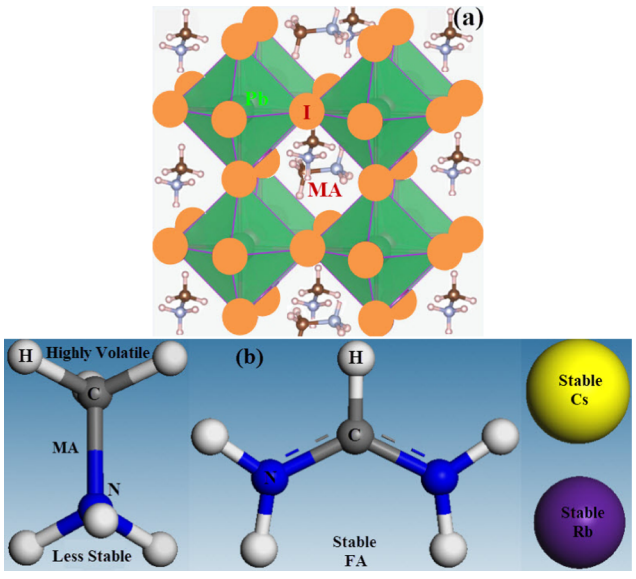

Figure 1. (a) Schematic supercell structure of $MAPbI_3$ taken with permission from the Journal of Materials Chemistry A as our previous work.[37] It contains eight Pb atoms inside the iodide octahedra, while the MA cation (CH_3NH_3) is at the center of the corner-sharing Pb/I octahedral cage. Relaxed crystal structures for a few materials are shown in the Supporting Information (Figure S1). (b) Schematic figure of the A-site cation (MA) is shown, which is less stable due to the highly volatile nature, which makes $MAPbI_3$ less stable. Therefore, to decrease the volatile nature of MA, we mixed stable Rb, Cs, and FA cations with MA.

IV. FORMABILITY, ENTHALPY FORMATION, AND MOLECULAR DYNAMIC SIMULATIONS

To introduce a new molecule/ion into a perovskite material, we have to investigate its formability by explaining the tolerance[32] and octahedral factor.[58] A modified form of the Goldschmidt tolerance factor was presented by G. Kieslich et al.[59,60] by introducing the effective ionic radii, $t_f = (r_{A,eff} + r_{X,eff})/\sqrt{2}(r_{B,eff} + r_{X,eff})$, where $r_{A,eff}$ and $r_{X,eff}$ represent the effective ionic radii for cation A and anion X, respectively, and $r_{B,eff}$ represents the B-site cation. We have used effective ionic radii for A-site cations (MA, FA, Cs, Rb)[20] and X-site anions (I, Br) and Shannon's radii[61] for B-site cations (Ca, Sr, Sn, Ge), as presented in Table. 1.

Table 1. Effective Ionic Radii for A-Site Cations[a]

A-site	r_{eff}	t_{APbI_3}	B-site	$r_{Shannon}$	X-site	r_{eff}
MA^{1+}	217	0.92	Ca^{2+}	100	I^{1-}	220
FA^{1+}	253	0.99	Sr^{2+}	118	Br^{1-}	196
Cs^{1+}	167	0.81	Ge^{2+}	73	Cl^{1-}	181
Rb^{1+}	152	0.79	Sn^{2+}	115		
			Pb^{2+}	119		

[a]On the basis of $r_{A,eff}$, the tolerance factors (t) for $APbI_3$ (A = MA, FA, Rb, Cs) are shown. $r_{Shannon}$ represents Shannon's effective ionic radii for B-site cations. X-site anions' effective ionic radii are also shown. Units for all of the radii (r_{eff}) are in picometer (pm).

According to Goldschmidt,[32] the perovskite phase will exist if the tolerance factor (t) is in the range of $0.8 \leq t \leq 1.0$. If the tolerance factor is higher or lower than this range, then the structure may not exist in the perovskite phase (unstable and photoinactive).[32,59,60] Distortion and tilting in the lead-halide cage will be created if the A-site cation is large[62] or too small,[63] which can make the structure less symmetric and photoinactive. A highly stable and photoactive cubic perovskite phase exists in the tolerance factor range of $0.9 \leq t \leq 1.0$. The tetragonal phase ($I4/mcm$, stable and photoactive, $t = 0.92$) of $MAPbI_3$ is carefully studied so far at normal temperature. Full details about the tolerance factor, octahedral tilting, and enthalpy formation for $MAPbI_3$ are given in the Supporting Information (Table.S2). Goldschmidt's tolerance factor (t) cannot perfectly explain the distortion/tilting, especially when we introduce a new ion at the B- or X-site of a perovskite. For this purpose, we have to explain the octahedral factor ($\mu = \frac{r_B}{r_X}$, range; $0.377 \leq \mu \leq 0.895$).[58] Octahedral factor/tilting will be produced if the B-site cation does not fit well with the X_6 octahedron, which is responsible for structural distortion/tilting and has a high impact on structural parameters too.[58]

It is obvious from the tolerance factor (t) values presented in Figure 2 that all of the predicted perovskite materials have less lattice distortion and hence exist in the range of the perovskite

https://dx.doi.org/10.1021/acsami.0c14595
ACS Appl. Mater. Interfaces 2020, 12, 49636−49647

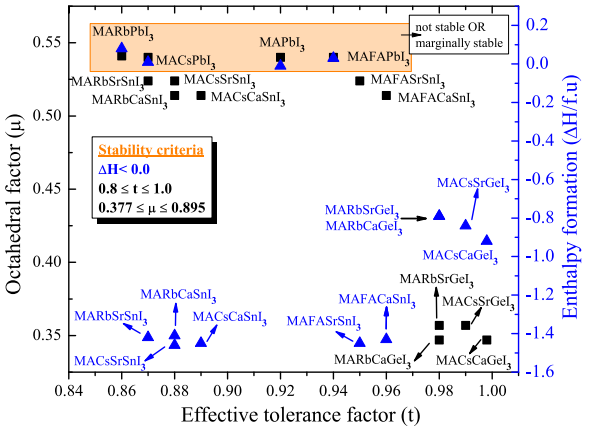

Figure 2. Black square symbols represent the tolerance factor (t_f) and octahedral factor (μ) values. Results show that all of the investigated Pb-free materials have perovskite phase stability. Blue triangle symbols indicate the enthalpy formation (ΔH) values for all of our predicted Pb-free and non-Pb-free perovskite materials. ΔH confirms the thermodynamic stability of all of the perovskites except for the Pb-containing materials as shown in the rectangular light-orange box. We can see that $MAPbI_3$ is marginally stable. The stability criteria for the tolerance factor, the octahedral factor, and enthalpy formation are shown inside the box.

phase. The same figure also states that germanium (Ge) mixed materials show a larger distortion, while the remaining perovskites have less octahedral distortion and tilting (still in the perovskite phase). The reason behind the larger distortion and tilting is due to the smaller ionic radii of germanium (r = 73 pm) as compared to other B-site mixed cations, as is clear from Table 1.

Figure 2 also shows the enthalpy formation (ΔH/f.u.) value, which is an important factor for the decomposition reaction (chemical stability) and thermodynamic stability of materials. It has been investigated that $MAPbI_3$ decomposes to MAI + PbI_2,[16] while for other Pb-based materials, the decomposition reactions are shown in Section SII (Supporting Information). The following decomposition reaction has been used in our triple-iodide (I_3) and mixed-halide (I_2Br_1) perovskites. $MA_nCs_{1-n}Sr_{1-b}Sn_bI_3$ and $MA_nCs_{1-n}Sr_{1-b}Sn_bI_2Br_1$ have been chosen as examples.

$$\Delta H = E(MA_nCs_{1-n}Sr_bSn_{1-b}I_3) - [nE(MAI) + (1-n)E(CsI) + bE(SrI_2) + (1-b)E(Sn) + cE(I_2)] \quad (1)$$

$$\Delta H = E(MA_nCs_{1-n}Sr_bSn_{1-b}I_2Br_1) - [nE(MABr) + (1-n)E(CsBr) + bE(SrI_2) + (1-b)E(Sn) + cE(I_2)] \quad (2)$$

where n, b, and c represent ratios 0.625, 0.125, and 0.875, respectively.

The enthalpy formation (ΔH) values obtained from the decomposition reactions in Figure 2 show that except for Pb-containing materials ($MARbPbI_3$, $MACsPbI_3$, $MAFAPbI_3$), all of the remaining predicted perovskites are thermodynamically stable. The more negative the ΔH value, the more stable will be the material. $MAPbI_3$ is marginally stable (ΔH = −0.01), which is consistent with the previous results (Supporting Information, Table.S2). Due to the more stable tolerance factor and octahedral values, all of the Sn-based perovskites have highly negative ΔH values and thus are stable enough. In the case of mixed-halide (I/Br) perovskites, the tolerance factor, octahedral factor, and enthalpy formation values are given in the Supporting Information (Figure S2), confirming that all Pb-free mixed-halide perovskites are stable enough. In our previous works,[27,37] where we studied only B-site mixing (Pb-free), we obtained less negative ΔH values; however, in this study, by mixing Rb, Cs, and FA cations with the A-site MA, the ΔH values were very negative. Therefore, we can say that not only B-site mixing (Pb-free) enhances the stability, but mixing Rb, Cs, and FA cations with MA (less stable) can also enhance the stability, as is obvious from Figure 2.

To further confirm the stability of these materials, we performed MD simulations. As MD calculations are very time-consuming, we selected three materials from pure triple iodide ($(MACs(CaSn)I_3$, $MARb(CaGe)I_3$, $MARb(SrGe)I_3)$) and only one from mixed iodide-bromide ($MAFA(SrSn)I_2Br_1$). From MD simulation plots (Fig.S3), the time-dependent evaluation of potential energies was found to oscillate within a narrow range, during the entire simulation time, indicating that these newly predicted HOIPs can maintain their structural stability at room temperature. In the case of a mixed-halide system ($MAFA(SrSn)I_2Br_1$), we can see little higher oscillations as compared to pure triple-iodide systems. This behavior may be attributed to the larger size of the FA cation, which distorts the structure further, confirming the larger deviation of the lattice parameters (Table.S1), or may be due to the highly correlated atomic motion. We can conclude that similar to the alloyed Sn or Pb materials, which appear to have unprecedented high stability, we also expect high stability for our alloyed systems (Ca/Ge,Sn; Sr/Ge,Sn).

IV.I. Electronic Properties. After successful relaxation of all of the perovskite structures, the lattice parameter values are given in the Supporting Information (Table.S1). The lattice volume decreases in Rb- and Cs-based perovskites as compared to the pristine $MAPbI_3$. This decrease (lattice constants decrease too) is basically due to the smaller ionic radii of Rb and Cs than that of MA, which reinforces the interaction between the organic cation and the octahedral cage; hence, the photostability and moisture stability are expected to increase.

Suitable and direct band-gap materials are in high demand in the PV industry. A theoretical study revealed that changes in the density of states occur due to the incorporation of different cations and anions at the X−Pb−X bond angle and length and also by changing the chemical composition, which results in tuning the band gap.[64] Band gaps higher than 2.0 eV and less than 0.9 eV are less efficient because most of the Sun radiations reaching the Earth's surface have energy less than 2 eV. Furthermore, materials having a band-gap range of 0.9−2.0 eV are suitable not only for single-junction solar cells but also for the top and bottom cells in the tandem architecture. Figures 3 and 4 show the band-gap values (HSE06) for all of our newly predicted Pb-free perovskite materials in comparison to $MAPbI_3$, $MARbPbI_3$, $MACsPbI_3$, and $MAFAPbI_3$, which have also been studied previously. Through HSE06 calculations, the band-gap value for $MAPbI_3$ is 2.20 eV, while the PBE band-gap value is 1.63 eV (Figure S4), well consistent with the experimental band-gap values of 1.50−1.70 eV.[41,65−69] Some previous results, as well as our own previous study, confirm that PBE gives accurate band-gap values only for lead (Pb)-containing ($MAPbX_3$; X = I,Br,Cl) perovskites,[70] while

https://dx.doi.org/10.1021/acsami.0c14595
ACS Appl. Mater. Interfaces 2020, 12, 49636−49647

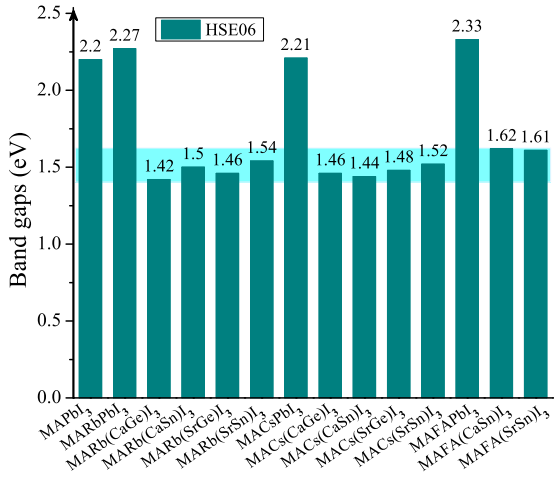

Figure 3. Band-gap values with HSE06 calculations for all of our predicted mixed A-site and B-site (Pb-free) perovskite materials. The LT cyan horizontal band represents an ideal range for the single-junction solar cells. Except for Pb-based perovskites, all of the remaining perovskites are in the optimum range (0.9−1.6 eV) of single-junction solar cells. Pb-containing perovskites have a large band gap and hence are suitable for the top cell in the tandem solar cell.

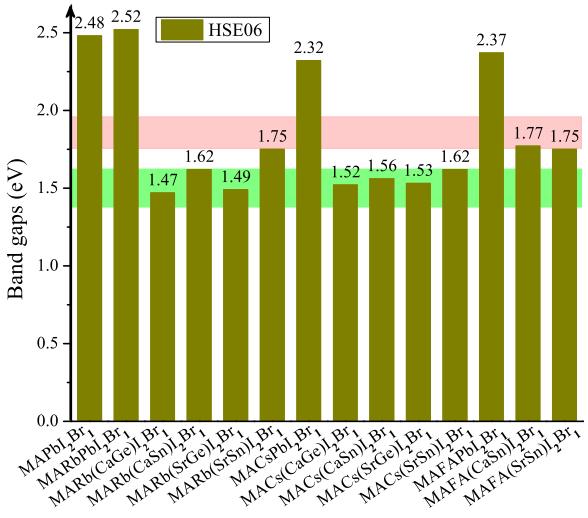

Figure 4. HSE06 band-gap values for all of our predicted mixed A-site, B-site (Pb-free), and X-site perovskite materials in comparison to $MAPbI_3$. The green horizontal band represents an ideal range for the single-junction solar cell, while the light-orange band represents the optimum band-gap range for the top cell in the tandem solar approach.

HSE06 overestimates the band gap in the case of Pb-containing perovskites.[27,37,71] Thus, from Figures 3 and 4, we can see very wide band gaps (>2.0 eV) in the case of Pb-containing perovskites. From our previous study,[27] in the case of monoreplacement Pb-free perovskites (especially Sn- and Ge-based), HSE06 gives very accurate band-gap values, well consistent with experimental results. The experimental band-gap value for $MA_{0.7}FA_{0.3}PbI_3$ is 1.58 eV,[72] while in our case, the HSE06 and PBE band-gap values for $MA_{0.625}FA_{0.375}PbI_3$ are 2.33 and 1.61 eV, respectively (Figures 3 and S4), which shows that the PBE value (1.61 eV) is well consistent with the experimental value (1.58 eV). From the above discussion, it is to be noted that the SOC effect can decrease the band-gap value by around 1.0 eV. If one includes the SOC effect along with the GW functional, then it is possible to obtain accurate band-gap values to that of the experimental one in the case of Pb-containing perovskites, but it is not sure to be possible in the case of PBE+SOC calculations.[42] It is to be noted that we did not include SOC effect in this study because (i) we replaced the B-site heavy element Pb with light elements Ca/Sr:Sn/Ge (showing smaller SOC effects) and (ii) it is very time-consuming for large data (total 28 materials) and large supercell (96 atoms) systems. In the mixed-halide approach (I/Br), the band-gap values increased on average by 0.1 eV (Figure 4) as compared to the pure triple-iodide (I_3) perovskites. All of our newly predicted perovskites show a direct band-gap nature at the γ (Γ) point. For our Pb-free mixed A-site and B-site cations, the band-gap values are in the range of 1.42−1.62 eV, an ideal range[73] for single-junction solar cells. The FA cation has a larger ionic radius than the MA cation does, which increases the lattice constants (clear from Table.S1) and consequently weakens the p−p hybridization due to the longer distance between atoms. Thus, the valence band maximum (VBM) shifts down and the band gap increases. The band structures of all of the studied Pb-free perovskites are shown in Figures 5 and S4 in comparison to $MAPbI_3$ and other Pb-based perovskites. From the band structure plots, we can see that the valance bands (VBs) of all of our predicted perovskites are highly dispersive as compared to the VBM of $MAPbI_3$, while the conduction band (CB) is not that dispersive. Band structures of the mixed B-site Sn-based perovskites are more dispersive as compared to the Ge- and Pb-based perovskites. It is seen that there are one to three dispersive energy bands at the VB and CB of our predicted Pb- and Ge-based perovskites, while the remaining bands are highly dense, especially at the VBM. This behavior was not observed in the Sn-based perovskites, where especially the valance band is highly dispersive. We cannot observe any big difference in the electronic properties due to alloying different A-site cations. Tunability of band gaps is observed in those A-, B-, and X-site alloyed materials, which have larger ionic radii.

It is to be noted that the more dispersive the VB and CB are, the lower the effective masses will be. The lower the effective masses are ($<1.0m_0$), the higher will be the carrier mobility, which is also an essential parameter for PV applications. Table. 2 shows the effective mass values for all of our Pb-free perovskite materials. All of our newly predicted perovskites show low hole and electron effective masses, which is responsible for the high electron and hole transport ability (mobility) of free charge carriers. The method for calculating the effective masses is shown in Section VII (Supporting Information).

We also calculated the reduced effective mass m_r^* ($1/m_r^* = 1/m_e^* + 1/m_h^*$), an important parameter for calculating the exciton binding energy (Table. 2). The exciton binding energy (E_b) is the energy required to dissociate excitons into free charge carriers before they can be collected. For PV applications, a smaller value of E_b is highly favorable to minimize the energy loss. This can be calculated using the Wannier equation[74]

$$E_b = \frac{m_r^*}{m_e}\frac{1}{\varepsilon_s^2}\frac{m_e e^4}{2(4\pi\varepsilon_0\hbar)^2} \approx 13.56\frac{m_r^*}{m_e}\frac{1}{\varepsilon_s^2}(\text{eV}) \quad (3)$$

where m_r^* is the reduced effective mass of excitons, m_e is the electron mass, ε_0 is the vacuum permittivity, e is the electron charge, ε_s is the static dielectric constant, and $\hbar$ is the Plank

https://dx.doi.org/10.1021/acsami.0c14595
ACS Appl. Mater. Interfaces 2020, 12, 49636−49647

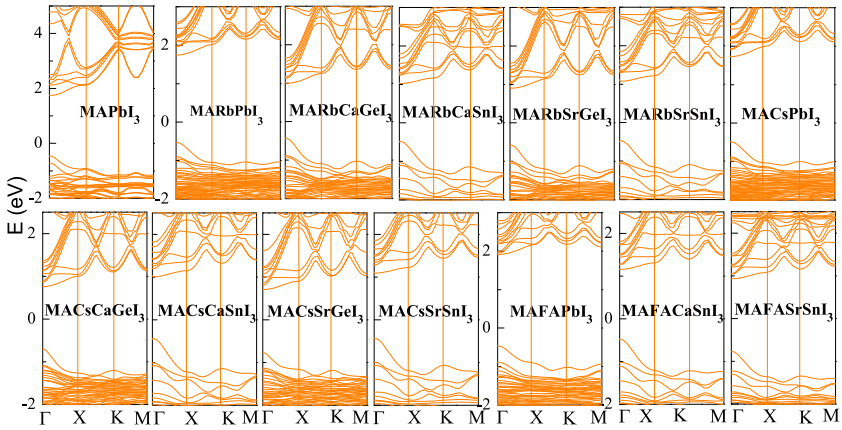

Figure 5. (a) Band structures for all of our predicted new perovskite materials with the HSE06 functional in comparison to $MAPbI_3$. In the case of Sn-based perovskites, the valance band is highly dispersive, while the conduction band is a bit dispersive in comparison to the Pb- and Ge-based perovskites.

Table 2. Effective Mass Values of Pb-Free Perovskite Materials,[b]

material	W	m_e^* (this)	m_h^* (this)	m_e^*(prev)	m_h^*(prev)	m_r^*	ε_s	E_b (this)	E_b (prev)
Si	3.69	0.25	0.13	0.19	0.16	0.086	13.59	0.69	15
GaAs	4.31	0.36	0.22	0.35	0.07	0.14	15.61	0.84	4.2
$MAPbI_3$	4.69	0.37	0.28	0.19,0.30	0.25,0.25	0.16	4.91	9.85	2−75,38,15
$MAPbI_2Br_1$	6.39	0.18	1.50			0.16	4.52	11.72	
$MARbPbI_3$	5.97	0.35	1.57			0.29	4.99	17.12	
$MARbPbI_2Br_1$	6.49	0.47	0.43			0.22	4.55	16.17	
$MARb(CaGe)I_3$	4.27	0.31	1.32			0.25	6.84	7.99	
$MARb(CaGe)I_2Br_1$	4.37	0.58	0.59			0.29	6.37	10.76	
$MARb(CaSn)I_3$	4.43	0.60	0.46			0.35	5.57	16.60	
$MARb(CaSn)I_2Br_1$	4.67	0.83	0.25			0.22	4.99	13.18	
$MARb(SrGe)I_3$	4.35	0.24	0.50			0.21	6.75	6.76	
$MARb(SrGe)I_2Br_1$	4.41	0.36	0.63			0.23	6.29	8.64	
$MARb(SrSn)I_3$	4.51	1.00	0.56			0.40	5.43	20.23	
$MARb(SrSn)I_2Br_1$	4.93	0.70	0.25			0.20	4.88	12.54	
$MACsPbI_3$	5.85	0.40	0.23			0.31	5.01	18.42	
$MACsPbI_2Br_1$	6.07	0.90	0.22			0.38	4.65	26.00	
$MACs(CaGe)I_3$	4.35	0.53	0.29			0.23	6.82	7.38	
$MACs(CaGe)I_2Br_1$	5.39	0.75	0.46			0.31	4.42	23.79	
$MACs(CaSn)I_3$	4.31	0.63	0.41			0.31	5.52	15.31	
$MACs(CaSn)I_2Br_1$	4.55	0.61	0.18			0.16	5.04	9.54	
$MACs(SrGe)I_3$	4.39	0.91	0.71			0.48	6.61	16.46	
$MACs(SrGe)I_2Br_1$	4.49	0.82	0.60			0.39	4.42	29.58	
$MACs(SrSn)I_3$	4.47	0.73	0.45			0.31	5.34	16.81	
$MACs(SrSn)I_2Br_1$	4.67	0.65	0.59			0.13	4.91	19.15	
$MAFAPbI_3$	6.05	0.15	0.91			0.11	4.91	7.97	
$MAFAPbI_2Br_1$	6.17	0.12	0.98			0.11	4.33	8.51	
$MAFA(CaSn)I_3$	4.67	0.91	0.37			0.26	5.10	15.08	
$MAFA(CaSn)I_2Br_1$	4.97	0.85	0.92			0.44	4.46	33.15	
$MAFA(SrSn)I_3$	4.65	0.94	0.42			0.29	4.88	18.13	
$MAFA(SrSn)I_2Br_1$	4.93	0.90	0.99			0.61	4.57	43.18	

[a]Here, "this" indicates the present study and "prev" is used for previous studies. [b]Electron−hole pair creation energy (W in eV), effective mass of electrons and holes (in units of bare electron mass m_0; $MAPbI_3$,[29] silicon,[42] GaAs[81]), reduced effective masses (m_r^*), static dielectric constants (ε_s), and exciton binding energy (E_b in meV; $MAPbI_3$,[3,68,75−79] silicon,[80] GaAs.[80]) for all of our simulated perovskite materials are presented with the present and previous results in comparison to Si, GaAs, and $MAPbI_3$.

constant. We calculated the exciton binding energy for all of our Pb-free perovskites in comparison to the previous values of $MAPbI_3$ (2−75, 38 meV),[3,68,75−79] silicon (15 meV),[80] and GaAs (4.2 meV).[80] We did not include excitonic effect in our calculations; thus, a minor error should be expected. Our calculated exciton binding energies for $MAPbI_3$ (9.58 meV) are well consistent with the previous theoretical and experimental results and close in the case of GaAs (4.2 meV), as shown in Table. 2. In the case of $MAPbI_3$, the experimental excitonic binding energy is higher than other conventional solar cell materials (as shown in Table. 2), but still $MAPbI_3$ has been investigated as an excitonic material. In

https://dx.doi.org/10.1021/acsami.0c14595
ACS Appl. Mater. Interfaces 2020, 12, 49636−49647

our calculations, the Ge-based Pb-free perovskites show a smaller excitonic binding energy, while Sn-base perovskites show comparably larger excitonic binding energies. $MAPbI_3$ (9.85 meV), $MAFAPbI_3$ (7.97 meV), and $MAFAPbI_2Br_1$ (8.51 meV) show smaller excitonic binding energies as compared to other materials. We expect that this low exciton binding energy is responsible for the photogenerated excitons dissociating spontaneously into free charge carriers, which further strengthens the long diffusion length of charge carriers. It is worth noting that in HOIPs, exciton dissociation is not a big issue. With E_b = 55 meV, almost 90% of the absorbed photons still lead to free charge carriers at exciton densities relevant to photovoltaics ($\sim 10^{16}$ cm^{-3}).[3]

Both $MAPbI_3$ and $MAPbI_2Br_1$ show strong p−p transition (I-p to Pb-p) from VB to CB (Supporting Information Figures S6 and 5), forming strong covalent bonding. This may be one of the reasons for their outstanding electronic properties. In all Sn-based perovskites, the transition is from the I-p to Sn-p orbitals except for $MACs(CaSn)I_3$, where the transition is from Sn-s to I-p (Supporting Information Fig.S6), and this is the reason why $MACs(CaSn)I_3$ show better dispersive nature (Figure 5). Ge-based Pb-free perovskites show the same transition behavior (I-p to Ge-p) to pristine $MAPbI_3$ (Supporting Information Fig.S6). The s−p and p−p transitions are responsible for low effective masses, which is one of the important factors in enhancing the charge carrier's mobility. In perovskite solar cells, the p−p transition is responsible for the strong optical absorption. Table. 2 shows that our calculated effective masses for $MAPbI_3$, Si, and GaAs are in good agreement with the previously calculated results.[29,42,81]

IV.II. Optical Properties and Absorption Efficiency. We calculated optical properties of all of the listed materials with the PBE functional and then used the scissors operator (for a detailed description, see section VIII, "scissors operator" in the Supporting Information) for the corrected optical properties, with a rigid shifting of the CB and VB, which alters the energy gap but retains the same dispersion. In fact, the PBE functional underestimates the optical band gap, which on the other hand overestimates the optical absorption.[82] The absorption coefficient is an important parameter of the material's optical absorption. Figures 6 and S7 (Supporting Information) show the absorption coefficient for all of our predicted perovskite materials in comparison to Si, GaAs (current leading PV partners), and $MAPbI_3$. All of our simulated Pb-free perovskites show strong absorption coefficient values similar to those of previously investigated absorption coefficients for $MAPbI_3$ (10^4−10^5 cm^{-1}), Si, and GaAs. The absorption coefficients of Si and GaAs are a little higher than that of $MAPbI_3$. All of our Pb-free materials show very sharp absorption edges, confirming their direct transition from VB to CB. In the case of mixed-halide perovskites (I/Br; Figure S7), the absorption coefficient decreases as compared to pure iodide (I_3)-based perovskites because of the Br incorporation. Mixing A-site (Rb, Cs, FA) cations in the Pb-based perovskites somewhat increases the optical band gap. Thus, the absorption curve moves to higher energies as compared to $MAPbI_3$, which decreases the optical absorption. In the case of B-site Sn- and Ge-based perovskites, Sn-based perovskites show a stronger optical absorption than the Ge-based ones, as is obvious from Figures 6, 7, and S7. It has been experimentally investigated that $Rb_{0.05}MA_{0.95}PbI_3$ has a stable efficiency of 18.8%;[31] thus, we expect high efficiency in our Pb-free study too, as seen from Figure 7. According to the AM 1.5 solar spectrum (shown in Figure 6), 98% of the light photons reaching the Earth's surface have energy below 4.0 eV. It is worth noting that all of our predicted Pb-free perovskite materials show high absorption below 4.0 eV (covering visible, infrared, and ultraviolet regions of the light spectrum); hence, we expect high absorption in these new perovskite materials.

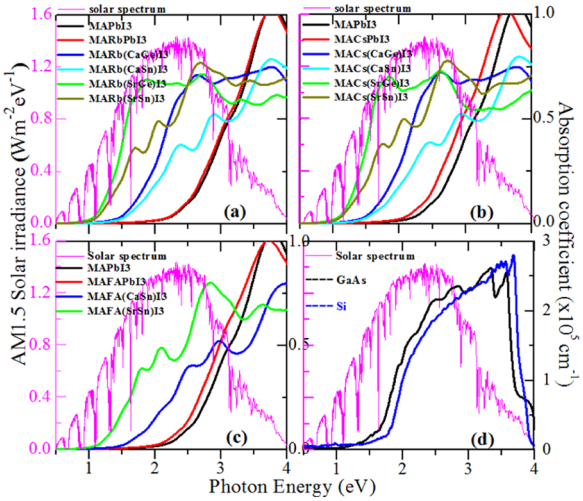

Figure 6. Absorption coefficient (α) plots for all of our new predicted Pb-free perovskite materials are shown in comparison to Si, GaAs, and $MAPbI_3$. AM 1.5-Solar spectral irradiance (Wm^{-2} eV^{-1}) has also been presented for comparison.

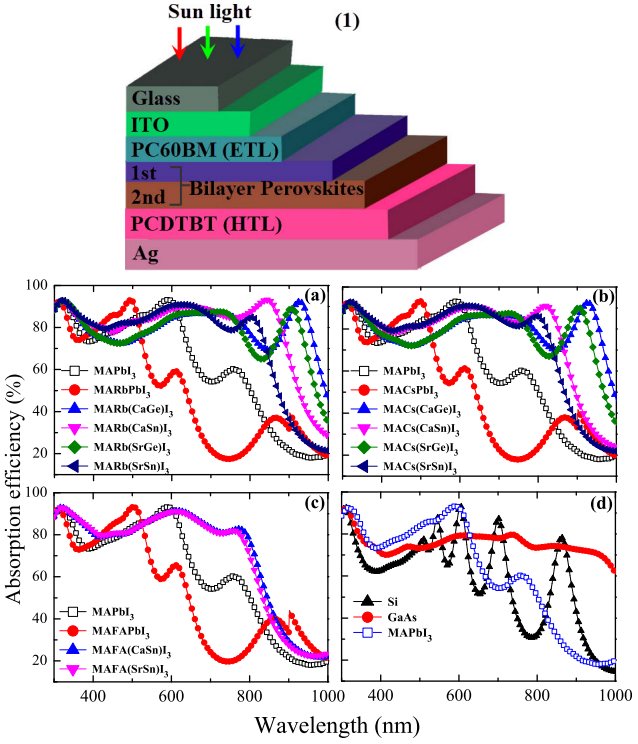

Figure 7. (1) Schematic figure of the simulated device structure for calculating the absorption efficiencies (bilayer) is shown, and the same device structure with a single layer was used for single layer's efficiencies. Full description of this device structure is provided in Section III of the Supporting Information. Single-layer device absorption efficiencies for all of our mixed A-site and B-site predicted Pb-free perovskite materials in comparison to $MAPbI_3$; for comparison, we also included Si and GaAs (PBE results).

https://dx.doi.org/10.1021/acsami.0c14595
ACS Appl. Mater. Interfaces 2020, 12, 49636−49647

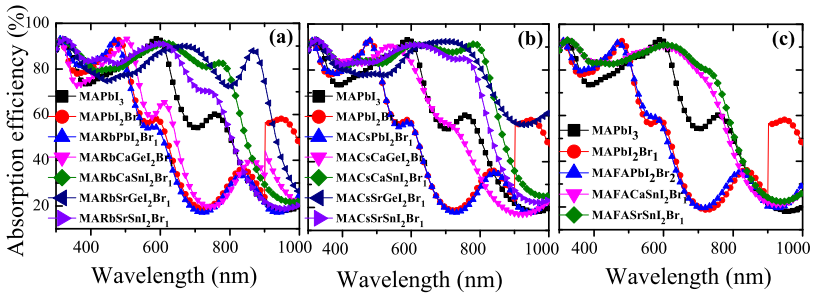

Figure 8. In comparison to Figure 7, the single-layer device absorption efficiencies decrease when we mixed X-site anions (I/Br). It is due to the increase of band gaps; the higher the Br ratio is, the higher will be the band gaps and hence the lower will be the efficiency. $MAPbI_3$ has also been presented for comparison.

Table. S3 (Supporting Information) shows the refractive index (n), extinction coefficient (k), and dielectric function (ε_1 and ε_2) values for all of our predicted perovskites in comparison to the present and previous values for Si, GaAs, and $MAPbI_3$. Our calculated optical results are well consistent with previous results (Table.S3).

Here, we are interested in the carrier collection efficiency, to see the strength of the optical absorption. Due to the absorption of incident photons, an electron−hole (e−h) pair will be generated. For electron−hole pair generation, the required average energy is known as the electron−hole pair generation energy (W). Using the empirical model proposed by Devanathan and co-authors,[83] $W = 2E_g + 1.43$, where E_g is the band gap of the material. For all of our listed perovskites, the electron−hole pair energy (W) values are shown in Table. 2. The higher the W value is, the lower the photovoltaic performance will be. We can see that the electron−hole pair creation energy for pristine $MAPbI_3$ (W = 4.63 eV, using PBE E_g = 1.63 eV) is higher than that for most of our Pb-free perovskite materials and is comparable to the energy for GaAs (4.31 eV). Pb-based perovskites and mixed FA-based perovskites show a little higher W values. The number of e−h pairs per photon absorbed in the material can be calculated by the internal quantum yield ($\eta = h\nu/W$). Assuming that all of the materials are exposed to the same light radiation, which absorbs the same photon energy, all of our new materials, especially pure iodide (I_3), Pb-free perovskites, and $MARbCaGeI_3$, show the highest internal quantum yield. This states that each absorbed photon can generate a separate e−h pair, which will be collected at the electrodes, leading to a higher charge carrier collection efficiency.[84] This will increase the internal quantum efficiency (IQE) to 100%, further enhancing the short-circuit current (J_{sc}) and open-circuit voltage (V_{oc}).[84,85]

As the absorption of these Pb-free perovskites is very strong, we further investigated their solar device performance. We made a single-junction solar cell device (Figure 7(1)) to study the absorption efficiency of these newly predicted Pb-free perovskites in comparison to $MAPbI_3$, Si, and GaAs. It is to be noted that in the case of $MAPbI_3$, we used the PBE dielectric constants for calculating their absorption efficiency because the PBE results (electronic and optical properties) are well consistent with the experimental results. From Figure 7a,b, the device absorption efficiencies for Pb-containing and Pb-free mixed A-site (Rb/MA, Cs/MA) cations are presented. Here, in the case of Pb-containing perovskites, the absorption efficiency is very low compared to the pure $MAPbI_3$ and our Pb-free study. We can see that for Sn-based perovskites at the B-site (Pb-free), the absorption efficiency is very smooth and high (>80%) above 900 nm of the light spectrum. In the case of Ge-based perovskites, the absorption window is very broad (1000 nm) but the absorption efficiency is less (>70%). For mixed A-site FA/MA and B-site Sn-based cations, the absorption efficiency is strong (>80%) in a wavelength range of 800 nm. Rb incorporation at the A-site also somewhat enhances the absorption efficiency compared to the Cs and FA incorporation. The absorption efficiency in our entire Pb-free study is very high and has a broad spectral window as compared to $MAPbI_3$. Although the absorption efficiency of GaAs is not that high (70−80%), the absorption window is very broad, which smoothly goes above >1000 nm of the light spectrum. In the case of mixed-halide (Figure 8) Pb-free perovskites, the absorption efficiencies are lower as compared to the pure iodide (I_3)-based perovskites; this is because of the wider band gaps, which result in bromide incorporation.

Single-junction solar cell is not a sound approach to achieve high absorption efficiency because photons with energies less than the band gap (sub-band gap loss ∼23%) and higher than the band gap (thermalization loss ∼29%) will not contribute at all. Due to thermalization, the excited electrons relax at the conduction band edge, which basically limits the absorption efficiency. To overcome these limitations, two-junction (or tandem) and multijunction solar cells make use of several absorber layers with different and suitable band gaps. On stacking different absorbing layers, photons with a high energy are absorbed by the material having a wider band-gap semiconductor and photons having a lower energy are allowed to pass through the top layer to reach a smaller band-gap semiconductor (bottom cell), leading to a more efficient use of solar energy. The top-cell material should have a wider band gap (1.6−2.5 eV), while the bottom-cell band gap should be narrow (0.9−1.4 eV). The ideal band-gap range for the top cell is 1.75 eV, while for the bottom cell it is 1.3 eV. To date, the perovskite tandem solar efficiency has reached 25%, higher than the established silicon single-junction solar cell. Our aim is to achieve absorption efficiency over 90% in a broad absorption window (>1000 nm), for which the only possible way is to use a tandem approach. Tandem architecture is a cost-effective approach to get a wider range of the light spectrum. In the tandem approach, it is worth noting that the top-cell material should be transparent or semitransparent to allow the light rays to reach the bottom cell.

Therefore, we use the bilayer tandem solar cell approach to further enhance the absorption efficiency. For avoiding the strain between the two stacking layers, we selected a combination of materials having the maximum matching lattice parameters. For the top cell, we selected the best

https://dx.doi.org/10.1021/acsami.0c14595
ACS Appl. Mater. Interfaces 2020, 12, 49636−49647

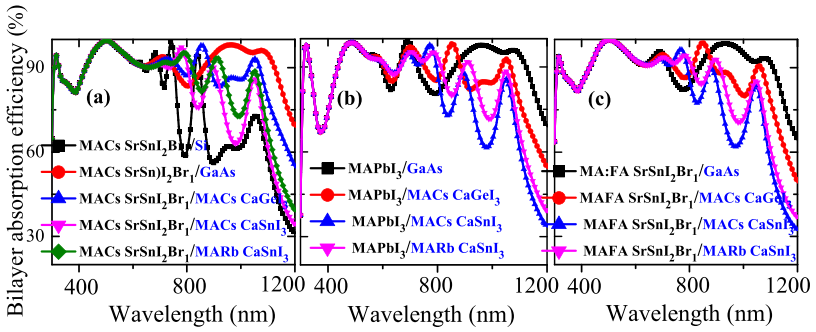

Figure 9. Bilayer (tandem solar cell) device absorption efficiencies are shown. We chose the best candidates from the single-junction solar cell approach as given in Figures 7 and 8 and then used them as tandem solar cells to further enhance their efficiencies. Top-layer (wide band gap) perovskites are shown in black, while bottom cells (narrow band gap) are shown in blue.

absorption efficiency perovskites from the single-junction approach with suitable band gaps, i.e., MACs(SrSn)I_2Br_1 (E_g = 1.62 eV), $MAPbI_3$ (PBE E_g = 1.63 eV), and MAFA(SrSn)-I_2Br_1 (E_g = 1.75 eV). Similarly, for the bottom cell, we also selected the best absorption materials (MACs(CaGe)I_3, 1.46 eV; MACs(CaSn)I_3, 1.44 eV; and MARb(CaSn)I_3, 1.5 eV) from the single-junction approach (Figure 7) along with the established PV Si and GaAs materials. It is obvious from Figure 9 that MACs(SrSn)I_2Br_1 (E_g = 1.62 eV) and $MAPbI_3$ (PBE E_g = 1.63 eV) as top cells give excellent absorption efficiencies (above 90%) in a wide range of the light spectrum (~1200 nm) with their bottom-cell counterparts as compared to the top-cell MAFA(SrSn)I_2Br_1 (E_g = 1.75 eV). In our previous theoretical bilayer study,[86] ($MAPbI_3$/GeSe) efficiency of 23.77% was achieved, which confirms that $MAPbI_3$ also acts well as a top cell with nonperovskite materials. Here, in the case of $MAPbI_3$ ($E_{g(PBE)}$ =1.63 eV) as a top cell, we can see an abrupt decrease (reaching below 70%) in the absorption in a short wavelength range of 300−400 nm, but after that, the efficiency goes higher and becomes smooth until 1100 nm of wavelength. Here, in our bilayer study, GaAs as a bottom cell shows the best absorption efficiency with their top cells as compared to other bottom solar cell materials (Figure 9). We also calculated the absorption efficiency in the case of MAFA(CaSn)I_2Br_1 as a suitable candidate material for the top cell with the above-mentioned bottom-cell materials (see Figure S8). In the tandem approach, the absorption window extended from 1000 nm (single-layer absorption) to 1200 nm with enhanced absorption efficiency (reaching 100% in some ranges of wavelengths), especially in $MAPbI_3$/GaAs and MACs(SrSn)I_2Br_1/GaAs. According to the above discussion, the absorption efficiency not only enhances (goes above 90%) but also covers the entire light spectrum (visible, infrared, and ultraviolet) reaching the Earth's surface. Thus, we can expect that these Pb-free perovskites have the potential to be used in realistic high-performance solar cells.

V. CONCLUSIONS

The aim of this study was to discover new environmentally friendly stable perovskite materials for sustainable and green energy applications. We investigated the incorporation of Rb, Cs, and FA with the MA cation at the A-site of 3D-$MAPbI_3$. The reason behind the A-site mixing was to decrease the volatile nature of the MA cation, which make it less stable. To achieve Pb-free stable perovskites, we mixed Ca/(Sn,Ge) and Sr/(Sn,Ge) at the B-site. To further enhance the stability, we mixed halide anions (I/Br). Enthalpy formation, MD simulations, and tolerance and octahedral factors confirm that all of our newly predicted perovskite materials are stable enough compared to pristine $MAPbI_3$. We observed that not only B- and X-site mixing increases the stability, but also A-site mixing was also responsible for their stability. The direct band-gap values (1.42−1.77 eV) for all of our mixed Pb-free perovskites are in the optimum range of single-junction and top-cell tandem approach. We observed that mixing halides (I/Br) tuned the band gap, which directly affects (decrease) the electronic and optical absorption. All of our Pb-free perovskite materials have highly dispersive VB and CB (smaller effective masses), which may result in high charge carrier mobility with excellent transport properties. Our calculated exciton binding energies for pristine $MAPbI_3$ and GaAs are well consistent with previous results. Most of our Ge-based perovskites have small exciton binding energies (<20 meV). Among the 28 total studied perovskite materials, Pb-free MARb/MACs(CaGe, CaSn)I_3 are found to have a strong and broad absorption in the single-junction approach. To overcome the thermalization and sub-band-gap losses, we used the tandem approach in which MACs(SrSn)I_2Br_1/GaAs and $MAPbI_3$/GaAs were found to be the best top/bottom combinations in this study for PV applications. The strong absorption efficiency (above 90%) in a wide spectral range (300−1200 nm) confirms their potential in the field of solar cells. This study will provide a new direction in designing stable Pb-free perovskite materials for green energy applications.

■ ASSOCIATED CONTENT

Supporting Information

The Supporting Information is available free of charge at https://pubs.acs.org/doi/10.1021/acsami.0c14595.

Crystal structures and their alloying, lattice parameters, methodology (device absorption efficiency), tolerance and octahedral factors, possible decomposition reactions, methodology (MD simulations), effective masses, scissors operator, dielectric constants, refractive index, and extinction coefficient (PDF)

■ AUTHOR INFORMATION

Corresponding Authors

Roshan Ali − *School of Electronic, Electrical and Communication Engineering and Theoretical Condensed Matter Physics and Computational Materials Physics Laboratory, School of Physical Sciences, University of Chinese Academy of Sciences, Beijing 100049, China; The Guo Photonics Laboratory, Changchun Institute of Optics, Fine Mechanics, and*

https://dx.doi.org/10.1021/acsami.0c14595
ACS Appl. Mater. Interfaces 2020, 12, 49636−49647

Physics, Chinese Academy of Sciences, Changchun 130033, China; orcid.org/0000-0001-7948-0833; Email: roshan@ciomp.ac.cn

Zhen-Gang Zhu − *School of Electronic, Electrical and Communication Engineering, Theoretical Condensed Matter Physics and Computational Materials Physics Laboratory, School of Physical Sciences, and CAS Center for Excellence in Topological Quantum Computation, University of Chinese Academy of Sciences, Beijing 100049, China;* orcid.org/0000-0002-2837-6072; Email: zgzhu@ucas.ac.cn

Gang Su − *Theoretical Condensed Matter Physics and Computational Materials Physics Laboratory, School of Physical Sciences, Kavli Institute for Theoretical Sciences, and CAS Center for Excellence in Topological Quantum Computation, University of Chinese Academy of Sciences, Beijing 100049, China*; Email: gsu@ucas.ac.cn

Chunlei Guo − *The Guo Photonics Laboratory, Changchun Institute of Optics, Fine Mechanics, and Physics, Chinese Academy of Sciences, Changchun 130033, China; The Institute of Optics, University of Rochester, Rochester, New York 14627, United States;* orcid.org/0000-0001-8525-6301; Email: guo@optics.rochester.edu

Authors

Qing-Bo Yan − *Theoretical Condensed Matter Physics and Computational Materials Physics Laboratory, School of Physical Sciences and College of Materials Science and Opto-Electronic Technology, University of Chinese Academy of Sciences, Beijing 100049, China;* orcid.org/0000-0002-1001-1390

Qing-Rong Zheng − *Theoretical Condensed Matter Physics and Computational Materials Physics Laboratory, School of Physical Sciences, University of Chinese Academy of Sciences, Beijing 100049, China*

Amel Laref − *Department of Physics and Astronomy, College of Science, King Saud University, Riyadh 11451, Saudi Arabia*

Chaudry Sajed Saraj − *The Guo Photonics Laboratory, Changchun Institute of Optics, Fine Mechanics, and Physics, Chinese Academy of Sciences, Changchun 130033, China*

Complete contact information is available at: https://pubs.acs.org/10.1021/acsami.0c14595

Notes

The authors declare no competing financial interest.

■ ACKNOWLEDGMENTS

R.A. was financially supported by the CAS-TWAS President's fellowship program for Ph.D. study. This work was also supported by the NSFC (Grant Nos. 11674317, 11834014, 91750205, and 11774340). Z.-G.Z and G.S. were supported in part by the National Key R&D Program of China (Grant No. 2018FYA0305800), the Strategic Priority Research Program of CAS (Grant No. XDB28000000), and the Beijing Municipal Science and Technology Commission (Grant No. Z118100004218001). Z.-G.Z. was supported by the Fundamental Research Funds for the Central Universities. The authors are also thankful to the National Key R&D Program of China (Grant No. 2016YFA0200400). R.A. and C.G. also acknowledge the support from the National Natural Science Foundation of China (NSFC, 91750205, 11774340), the National Key Research and Development Program of China (2017YFB1104700, 2018YFB1107202), the K.C.W. Education Foundation (GJTD-2018-08), The Key Program of the International Partnership Program of CAS (181722KYSB20160015), and the Jilin Science and Technology Department Project (20180414019GH). This research project (for A.L.) was also supported by a grant from the "Research Centre of the Female Scientific and Medical Colleges", Deanship of Scientific Research, King Saud University.

■ REFERENCES

(1) NREL. Best Research-Cell Efficiencies. https://www.nrel.gov/pv/assets/pdfs/best-research-cell-efficiencies.20190802.pdf (accessed Dec 2019).

(2) De Wolf, S.; Holovsky, J.; Moon, S.-J.; Löper, P.; Niesen, B.; Ledinsky, M.; Haug, F.-J.; Yum, J.-H.; Ballif, C. Organometallic Halide Perovskites: Sharp Optical Absorption Edge and Its Relation to Photovoltaic Performance. *J. Phys. Chem. Lett.* **2014**, *5*, 1035.

(3) D'Innocenzo, V.; Grancini, G.; Alcocer, M. J. P.; Kandada, A. R. S.; Stranks, S. D.; Lee, M. M.; Lanzani, G.; Snaith, H. J.; Petrozza, A. Excitons versus free charges in organo-lead tri-halide perovskites. *Nat. Commun.* **2014**, *5*, No. 3586.

(4) Wehrenfennig, C.; Eperon, G. E.; Johnston, M. B.; Snaith, H. J.; Herz, L. M. High charge carrier mobilities and lifetimes in organolead trihalide perovskites. *Adv. Mater.* **2014**, *26*, 1584.

(5) Stranks, S. D.; Eperon, G. E.; Grancini, G.; Menelaou, C.; Alcocer, M. J. P.; Leijtens, T.; Herz, L. M.; Petrozza, A.; Snaith, H. J. Electron-Hole Diffusion Lengths Exceeding 1 Micrometer in an Organometal Trihalide Perovskite Absorber. *Science* **2013**, *342*, 341.

(6) Brandt, R. E.; Stevanovic, V.; Ginley, D. S.; Buonassisi, T. Identifying defect-tolerant semiconductors with high minority-carrier lifetimes: beyond hybrid lead halide perovskites. *MRS Commun.* **2015**, *5*, 265.

(7) Walsh, A.; Scanlon, D. O.; Chen, S.; Gong, X. G.; Wei, S.-H. Self-Regulation Mechanism for Charged Point Defects in Hybrid Halide Perovskites. *Angew. Chem.* **2015**, *127*, 1811.

(8) Deng, Y.; Peng, E.; Shao, Y.; Xiao, Z.; Dong, Q.; Huang, J. Scalable fabrication of efficient organolead trihalide perovskite solar cells with doctor-bladed active layers. *Energy Environ. Sci.* **2015**, *8*, 1544.

(9) Xing, G.; Mathews, N.; Sun, S.; Lim, S. S.; Lam, Y. M.; Grätzel, M.; Mhaisalkar, S.; Sum, T. C. Long-range balanced electron- and hole-transport lengths in organic-inorganic $CH_3NH_3PbI_3$. *Science* **2013**, *342*, 344.

(10) Ganose, A. M.; Savory, C. N.; Scanlon, D. O. Beyond methylammonium lead iodide: prospects for the emergent field of ns^2 containing solar absorbers. *Chem. Commun.* **2017**, *53*, 20.

(11) Barrows, A. T.; Pearson, A. J.; Kwak, C. K.; Dunbar, A. D. F.; Buckley, A. R.; Lidzey, D. G. Efficient planar heterojunction mixed-halide perovskite solar cells deposited via spray-deposition. *Energy Environ. Sci.* **2014**, *7*, 2944.

(12) Tan, Z.-K.; Moghaddam, R. S.; Lai, M. L.; Docampo, P.; Higler, R.; Deschler, F.; Price, M.; Sadhanala, A.; Pazos, L. M.; Credgington, D.; Hanusch, F.; Bein, T.; Snaith, H. J.; friend, R. H. Bright light-emitting diodes based on organometal halide perovskite. *Nat. Nanotechnol.* **2014**, *9*, 687−692.

(13) Zhu, H.; Fu, Y.; Meng, F.; Wu, X.; Gong, Z.; Ding, Q.; Gustafsson, M. V.; Trinh, M. T.; Jin, S.; Zhu, X.-Y. Lead halide perovskite nanowire lasers with low lasing thresholds and high quality factors. *Nat. Mater.* **2015**, *14*, 636−642.

(14) Dou, L.; Yang, Y.; You, J.; Hong, Z.; Chang, W.-H.; Li, G.; Yang, Y. Solution-processed hybrid perovskite photodetectors with high detectivity. *Nat. Commun.* **2014**, *5*, No. 5404.

(15) Lee, Y.; Kwon, J.; Hwang, E.; Ra, C.-H.; Yoo, W. J.; Ahn, J.-H.; Park, J. H.; Cho, J. H. High-Performance Perovskite-Graphene Hybrid Photodetector. *Adv. Mater.* **2015**, *27*, 41−46.

(16) Juarez-Perez, E. J.; Hawash, Z.; Raga, S. R.; Ono, L. K.; Qi, Y. B. Thermal degradation of $CH_3NH_3PbI_3$ perovskite into NH_3 and CH_3I gases observed by coupled thermogravimetrymass spectrometry analysis. *Energy Environ. Sci.* **2016**, *9*, 3406−3410.

(17) Pellet, N.; Gao, P.; Gregori, G.; Yang, T.-Y.; Nazeeruddin, M. K.; Maier, J.; Grätzel, M. Mixed-organic-cation perovskite photovoltaics for enhanced solar-light harvesting. *Angew. Chem., Int. Ed.* **2014**, *53*, 3151−3157.
(18) Lee, J. W.; Kim, D.-H.; Kim, H.-S.; Seo, S.-W.; Cho, S. M.; Park, N.-G. Formamidinium and Cesium Hybridization for Photo- and Moisture-Stable Perovskite Solar Cell. *Adv. Energy Mater.* **2015**, *5*, No. 1501310.
(19) McMeekin, D. P.; Sadoughi, G.; Rehman, W.; Eperon, G. E.; Saliba, M.; Hörantner, M. T.; Haghighirad, A.; Sakai, N.; Korte, L.; Rech, B.; Johnston, M. B.; Herz, L. M.; Snaith, H. J. A mixed-cation lead mixed-halide perovskite absorber for tandem solar cells. *Science* **2016**, *351*, 151−155.
(20) Saliba, M.; Matsui, T.; Domanski, K.; Seo, J.-Y.; Ummadisingu, A.; Zakeeruddin, S. M.; Correa-Baena, J. P. C.; Tress, W. R.; Abate, A.; Hagfeldt, A.; Gratzel, M. Incorporation of rubidium cations into perovskite solar cells improves photovoltaic performance. *Science* **2016**, *354*, 206−209.
(21) Saliba, M.; Matsui, T.; Seo, J.-Y.; Domanski, K.; Correa-Baena, J.-P.; Nazeeruddin, M. K.; Zakeeruddin, S. M.; Tress, W.; Abate, A.; Hagfeldt, A.; Grätzel, M. Cesium-containing triple cation perovskite solar cells: improved stability, reproducibility and high efficiency. *Energy Environ. Sci.* **2016**, *9*, 1989−1997.
(22) Conings, B.; Drijkoningen, J.; Gauquelin, N.; Babayigit, A.; D'Haen, J.; D'Olieslaeger, L.; Ethirajan, A.; Verbeeck, J.; Manca, J.; Mosconi, E.; Angelis, F. D.; Boyen, H.-G. Intrinsic Thermal Instability of Methylammonium Lead Trihalide Perovskite. *Adv. Energy Mater.* **2015**, *5*, No. 1500477.
(23) Lee, J.-W.; Seol, D.-J.; Cho, A.-N.; Park, N.-G. High-Efficiency Perovskite Solar Cells Based on the Black Polymorph of HC$(NH_2)_2PbI_3$. *Adv. Mater.* **2014**, *26*, 4991−4998.
(24) Jeon, N. J.; Noh, J. H.; Yang, W. S.; Kim, Y. C.; Ryu, S.; Seo, J.; Seok, S. I. Compositional engineering of perovskite materials for high-performance solar cells. *Nature* **2015**, *517*, 476−480.
(25) Bi, D. Q.; Yi, C.; Luo, J.; Décoppet, J.-D.; Zhang, F.; Zakeeruddin, S. M.; Li, X.; Hagfeldt, A.; Grätzel, M. Polymer-templated nucleation and crystal growth of perovskite films for solar cells with efficiency greater than 21%. *Nat. Energy* **2016**, *1*, 16142.
(26) Noh, J. H.; Im, S. H.; Heo, J. H.; Mandal, T. N.; Seok, S. I. Chemical Management for Colorful, Efficient, and Stable Inorganic-Organic Hybrid Nanostructured Solar Cells. *Nano Lett.* **2013**, *13*, 1764−1769.
(27) Ali, R.; Hou, G.-J.; Zhu, Z.-G.; Yan, Q.-B.; Zheng, Q.-R.; Su, G. Predicted Lead-Free Perovskites for Solar Cells. *Chem. Mater.* **2018**, *30*, 718−728.
(28) Yang, W. S.; Noh, J. H.; Jeon, N. J.; Kim, Y. C.; Ryu, S.; Seo, J.; Seok, S. I. High-performance photovoltaic perovskite layers fabricated through intramolecular exchange. *Science* **2015**, *348*, 1234−1237.
(29) Wang, Z.; Lin, Q.; Chmiel, F. P.; Sakai, N.; Herz, L. M.; Snaith, H. J. Efficient ambient-air-stable solar cells with 2D-3D heterostructured butylammonium-caesium-formamidinium lead halide perovskites. *Nat. Energy* **2017**, *2*, No. 17135.
(30) Turren-Cruz, S.-H.; Hagfeldt, A.; Saliba, M. Methylammonium-free, high-performance, and stable perovskite solar cells on a planar architecture. *Science* **2018**, *362*, 449−453.
(31) Park, I. J.; Seo, S.; Park, M. A.; Lee, S.; Kim, D. H.; Zhu, K.; Shin, H.; Kim, J. Y. Effect of Rubidium Incorporation on the Structural, Electrical, and Photovoltaic Properties of Methylammonium Lead Iodide-Based Perovskite Solar Cells. *ACS Appl. Mater. Interfaces* **2017**, *9*, 41898−41905.
(32) Goldschmidt, V. M. Die Gesetze der Krystallochemie. *Naturwissenschaften* **1926**, *14*, 477−485.
(33) Wang, Q.; Dong, Q.; Li, T.; Gruverman, A.; Huang, J. Thin Insulating Tunneling Contacts for Efficient and Water-Resistant Perovskite Solar Cells. *Adv. Mater.* **2016**, *28*, 6734−6739.
(34) Yang, Z.; Rajagopal, A.; Chueh, C.-C.; Jo, S. B.; Liu, B.; Zhao, T.; Jen, A. K. Y. Stable Low-Bandgap Pb-Sn Binary Perovskites for Tandem Solar Cells. *Adv. Mater.* **2016**, *28*, 8990−8997.
(35) Eperon, G. E.; Leijtens, T.; Bush, K. A.; Prasanna, R.; Green, T.; Wang, J. T. W.; McMeekin, D. P.; Volonakis, G.; Milot, R. L.; May, R.; Palmstrom, A.; Slotcavage, D. J.; Belisle, R. A.; Patel, J. B.; Parrott, E. S.; Sutton, R. J.; Ma, W.; Moghadam, F.; Conings, B.; Babayigit, A.; Boyen, H. G.; Bent, S.; Giustino, F.; Herz, L. M.; Johnston, M. B.; McGehee, M. D.; Snaith, H. J. Perovskite-perovskite tandem photovoltaics with optimized band gaps. *Science* **2016**, *354*, 861−865.
(36) Klug, M. T.; Osherov, A.; Haghighirad, A. A.; Stranks, S. D.; Brown, P. R.; Bai, S.; Wang, J. T.-W.; Dang, X.; Bulovic, V.; Snaith, H. J.; Belcher, A. M. Tailoring metal halide perovskites through metal substitution: influence on photovoltaic and material properties. *Energy Environ. Sci.* **2017**, *10*, 236−246.
(37) Ali, R.; Hou, G.-J.; Zhu, Z.-G.; Yan, Q.-B.; Zheng, Q.-R.; Su, G. Stable mixed group II (Ca, Sr) and XIV (Ge, Sn) lead-free perovskite solar cells. *J. Mater. Chem. A* **2018**, *6*, 9220.
(38) Swarnkar, A.; Mir, W. J.; Nag, A. Can B-Site Doping or Alloying Improve Thermal- and Phase-Stability of All-Inorganic $CsPbX_3$ (X = Cl, Br, I) Perovskites. *ACS Energy Lett.* **2018**, *3*, 286−289.
(39) Song, T.-B.; Yokoyama, T.; Stoumpos, C. C.; Logsdon, J.; Cao, D. H.; Wasielewski, M. R.; Aramaki, S.; Kanatzidis, M. G. Importance of Reducing Vapor Atmosphere in the Fabrication of Tin-Based Perovskite Solar Cells. *J. Am. Chem. Soc.* **2017**, *139*, 836−842.
(40) Liao, Y.; Liu, H.; Zhou, W.; Yang, D.; Shang, Y.; Shi, Z.; Li, B.; Jiang, X.; Zhang, L.; Quan, L. N.; Quintero-Bermudez, R.; Sutherland, B. R.; Mi, Q.; Sargent, E. H.; Ning, Z. Highly Oriented Low-Dimensional Tin Halide Perovskites with Enhanced Stability and Photovoltaic Performance. *J. Am. Chem. Soc.* **2017**, *139*, 6693−6699.
(41) Stoumpos, C. C.; Malliakas, C. D.; Kanatzidis, M. G. Semiconducting Tin and Lead Iodide Perovskites with Organic Cations: Phase Transitions, High Mobilities, and Near-Infrared Photoluminescent Properties. *Inorg. Chem.* **2013**, *52*, 9019−9038.
(42) Umari, P.; Mosconi, E.; Angelis, F. D.; Relativistic, G. W. calculations on $CH_3NH_3PbI_3$ and $CH_3NH_3SnI_3$ perovskites for solar cell applications. *Sci. Rep.* **2014**, *4*, No. 4467.
(43) Koh, T. M.; Krishnamoorthy, T.; Yantara, N.; Shi, C.; Leong, W. L.; Boix, P. P.; Grimsdale, A. C.; Mhaisalkar, S. G.; Mathews, N. Formamidinium tin-based perovskite with low Eg for photovoltaic applications. *J. Mater. Chem. A* **2015**, *3*, 14996−15000.
(44) Li, C.; Song, Z.; Zhao, D.; Xiao, C.; Subedi, B.; Shrestha, N.; Junda, M. M.; Wang, C.; Jiang, C.-S.; Al-Jassim, M.; Ellingson, R. J.; Podraza, N. J.; Zhu, K.; Yan, Y. Reducing Saturation-Current Density to Realize High-Efficiency Low-Bandgap Mixed Tin-Lead Halide Perovskite Solar Cells. *Adv. Energy Mater.* **2019**, *9*, No. 1803135.
(45) Hao, F.; Stoumpos, C. C.; Chang, R. P. H.; Kanatzidis, M. G. Anomalous Band Gap Behavior in Mixed Sn and Pb Perovskites Enables Broadening of Absorption Spectrum in Solar Cells. *J. Am. Chem. Soc.* **2014**, *136*, 8094−8099.
(46) Shen, Q.; Ogomi, Y.; Chang, J.; Toyoda, T.; Fujiwara, K.; Yoshino, K.; Sato, K.; Yamazaki, K.; Akimoto, M.; Kuga, Y.; Katayamad, K.; Hayase, S. Optical absorption, charge separation and recombination dynamics in Sn/Pb cocktail perovskite solar cells and their relationships to photovoltaic performances. *J. Mater. Chem. A* **2015**, *3*, 9308−9316.
(47) Kapil, G.; Ripolles, T. S.; Hamada, K.; Ogomi, Y.; Bessho, T.; Kinoshita, T.; Chantana, J.; Yoshino, K.; Shen, Q.; Toyoda, T.; Minemoto, T.; Murakami, T. N.; Segawa, H.; Hayase, S. Highly Efficient 17.6% Tin-Lead Mixed Perovskite Solar Cells Realized through Spike Structure. *Nano Lett.* **2018**, *18*, 3600−3607.
(48) Sun, P.-P.; Li, Q.-S.; Feng, S.; Li, Z.-S. Mixed Ge/Pb perovskite light absorbers with an ascendant efficiency explored from theoretical view. *Phys. Chem. Chem. Phys.* **2016**, *18*, 14408−14418.
(49) Sun, Y.-Y.; Shi, J.; Lian, J.; Gao, W.; Agiorgousis, M. L.; Zhangde, P.; Zhang, S. Discovering lead-free perovskite solar materials with a split-anion approach. *Nanoscale* **2016**, *8*, 6284−6289.
(50) Giorgi, G.; Koichi, Y. Alternative, Lead-free, Hybrid Organic-Inorganic Perovskites for Solar Applications: A DFT Analysis. *Chem. Lett.* **2015**, *44*, 826−828.

https://dx.doi.org/10.1021/acsami.0c14595
ACS Appl. Mater. Interfaces 2020, 12, 49636−49647

(51) Lau, C. F. J.; Zhang, M.; Deng, X.; Zheng, J.; Bing, J.; Ma, Q.; Kim, J.; Hu, L.; Green, M. A.; Huang, S.; H-.Baillie, A. W. Y. Strontium-Doped Low-Temperature-Processed $CsPbI_2Br$ Perovskite Solar Cells. *ACS Energy Lett.* **2017**, *2*, 2319−2325.
(52) Pérez-Del-Rey, D.; Hutter, E. M.; Savenije, T. J.; Nordlund, D.; Schulz, P.; Berry, J. J.; Sessolo, M.; Bolink, H. J.; Forgács, D. Strontium Insertion in Methylammonium Lead Iodide: Long Charge Carrier Lifetime and High Fill-Factor Solar Cells. *Adv. Mater.* **2016**, *28*, 9839−9845.
(53) Yeh, J. W.; Chen, S. K.; Lin, S. J.; Gan, J. Y.; Chin, T. S.; Shun, T. T.; Tsau, C.-H.; Chang, S.-Y. Nanostructured High-Entropy Alloys with Multiple Principal Elements: Novel Alloy Design Concepts and Outcomes. *Adv. Eng. Mater.* **2004**, *6*, 299−303.
(54) Kresse, G.; Furthmüler, J. Efficiency of ab-initio total energy calculations for metals and semiconductors using a plane-wave basis set. *Comput. Mater. Sci.* **1996**, *6*, 15−50.
(55) Perdew, J. P.; Burke, K.; Ernzerhof, M. Generalized Gradient Approximation Made Simple. *Phys. Rev. Lett.* **1996**, *77*, 3865.
(56) Heyd, J.; Scuseria, G. E. Hybrid functionals based on a screened Coulomb potential. *J. Chem. Phys.* **2003**, *118*, 8207.
(57) Jia, W.; Cao, Z.; Wang, L.; Fu, J.; Chi, X.; Wang, L.-W.; Gao, W. The analysis of a plane wave pseudopotential density functional theory code on a GPU machine. *Comput. Phys. Commun.* **2013**, *84*, 9−18.
(58) Green, M. A.; H.-Baillie, A.; Snaith, H. J. The emergence of perovskite solar cells. *Nat. Photonics* **2014**, *8*, 506−514.
(59) Kieslich, G.; Sun, S.; Cheetham, A. K. Solid-state principles applied to organic-inorganic perovskites: new tricks for an old dog. *Chem. Sci.* **2014**, *5*, 4712−4715.
(60) Kieslich, G.; Sun, S.; Cheetham, T. An extended Tolerance Factor approach for organic-inorganic perovskites. *Chem. Sci.* **2015**, *6*, 3430−3433.
(61) Shannon, R. D. Revised effective ionic radii and systematic studies of interatomic distances in halides and chalcogenides. *Acta Crystallogr. A* **1976**, *A32*, 751−767.
(62) Borriello, I.; Cantele, G.; Ninno, D. Ab initio investigation of hybrid organic-inorganic perovskites based on tin halides. *Phys. Rev. B: Condens. Matter Mater. Phys.* **2008**, *77*, 235214.
(63) Da Silva, E. L.; Skelton, J. M.; Parker, S. C.; Walsh, A. Phase stability and transformations in the halide perovskite $CsSnI_3$. *Phys. Rev. B: Condens. Matter Mater. Phys.* **2015**, *91*, 144107.
(64) Filip, M. R.; Eperon, G. E.; Snaith, H. J.; Giustino, F. Steric engineering of metal-halide perovskites with tunable optical band gaps. *Nat. Commun.* **2014**, No. 5757.
(65) Kim, H. S.; Lee, C. R.; Im, J. H.; Lee, K. B.; Moehl, T.; Marchioro, A.; Moon, S. J.; H.-Baker, R.; Yum, J. H.; Moser, J. E.; Grätzel, M.; Park, N.-G. Lead Iodide Perovskite Sensitized All-Solid-State Submicron Thin Film Mesoscopic Solar Cell with Efficiency Exceeding 9%. *Sci. Rep.* **2012**, *2*, No. 591.
(66) Colella, S.; Mosconi, E.; Fedeli, P.; Listorti, A.; Gazza, F.; Orlandi, F.; Ferro, P.; Besagni, T.; Rizzo, A.; Calestani, G.; Giuseppe, G.; Angelis, F. D.; Mosca, R. $MAPbI_{3-x}Cl_x$ Mixed Halide Perovskite for Hybrid Solar Cells: The Role of Chloride as Dopant on the Transport and Structural Properties. *Chem. Mater.* **2013**, *25*, 4613−4618.
(67) Hirasawa, M.; Ishihara, T.; Goto, T. Exciton Features in 0-, 2-, and 3-Dimensional Networks of $[PbI_6]^{4-}$ Octahedra. *J. Phys. Soc. Jpn.* **1994**, *63*, 3870−3879.
(68) Tanaka, K.; Takahashi, T.; Ban, T.; Kondo, T.; Uchida, K.; Miura, N. Comparative study on the excitons in lead-halide-based perovskite-type crystals $CH_3NH_3PbBr_3$, $CH_3NH_3PbI_3$. *Solid State Commun.* **2003**, *127*, 619−623.
(69) Lindblad, R.; Bi, D.; Park, B.; Oscarsson, J.; Gorgoi, M.; Siegbahn, H.; Odelius, M.; Johansson, E. M. J.; Rensmo, H. Electronic Structure of $TiO_2/CH_3NH_3PbI_3$ Perovskite Solar Cell Interfaces. *J. Phys. Chem. Lett.* **2014**, *5*, 648−653.
(70) Zhang, Z.; Long, R.; Tokina, M. V.; Prezhdo, O. V. Interplay between Localized and Free Charge Carriers Can Explain Hot Fluorescence in the $CH_3NH_3PbBr_3$ Perovskite: Time-Domain Ab Initio Analysis. *J. Am. Chem. Soc.* **2017**, *139*, 17327−17333.
(71) Yang, D.; Lv, J.; Zhao, X.; Xu, Q.; Fu, Y.; Zhan, Y.; Zunger, A.; Zhang, L. Functionality-Directed Screening of Pb-Free Hybrid Organic-Inorganic Perovskites with Desired Intrinsic Photovoltaic Functionalities. *Chem. Mater.* **2017**, *29*, 524−538.
(72) Zhao, D.; Yu, Y.; Wang, C.; Liao, W.; Shrestha, N.; Grice, C. R.; Cimaroli, A. J.; Guan, L.; Ellingson, R. J.; Zhu, K.; Zhao, X.; Xiong, R.-G.; Yan, Y. Low-bandgap mixed tin-lead iodide perovskite absorbers with long carrier lifetimes for all-perovskite tandem solar cells. *Nat. Energy* **2017**, *2*, 17018.
(73) Ju, M.-G.; Chen, M.; Zhou, Y.; Garces, H. F.; Dai, J.; Ma, L.; Padture, N. P.; Zeng, X. C. Earth-Abundant Nontoxic Titanium(IV)-based Vacancy-Ordered Double Perovskite Halides with Tunable 1.0 to 1.8 eV Bandgaps for Photovoltaic Applications. *ACS Energy Lett.* **2018**, *3*, 297−304.
(74) Grundmann, M. *The Physics of Semiconductor*; Springer, 2006.
(75) Lin, Q.; Armin, A.; Nagiri, R. C. R.; Burn, P. L.; Meredith, P. Electro-optics of perovskite solar cells. *Nat. Photonics* **2015**, *9*, 106−112.
(76) Hirasawa, M.; Ishihara, T.; Goto, T.; Uchida, K.; Miura, N. Magnetoabsorption of the lowest exciton in perovskite-type compound $(CH_3NH_3)PbI_3$. *Phys. B* **1994**, *201*, 427−430.
(77) Ishihara, T. Optical properties of PbI-based perovskite structures. *J. Lumin.* **1994**, *60*, 269−274.
(78) Saba, M.; Cadelano, M.; Marongiu, D.; Chen, F.; Sarritzu, V.; Sestu, N.; Figus, C.; Aresti, M.; Piras, R.; Lehmann, A. G.; Cannas, C.; Musinu, A.; Quochi, F.; Mura, A.; Bongiovanni, G. Correlated electron-hole plasma in organometal perovskites. *Nat. Commun.* **2014**, *5*, No. 5049.
(79) Umari, P.; Mosconi, E.; Angelis, F. D. Infrared Dielectric Screening Determines the Low Exciton Binding Energy of Metal-Halide Perovskites. *J. Phys. Chem. Lett.* **2018**, *9*, 620−627.
(80) Pelant, I.; Valenta, J. Band Parameters for III−V Compound Semiconductors and their Alloys, In *Luminescence Spectroscopy of Semiconductors*; Oxford Univ. Press, 2012.
(81) Vurgaftman, I.; Meyer, J. R.; Ram-Mohan, L. R. Electro-optic Response in Germanium Halide Perovskites. *J. Appl. Phys.* **2001**, *89*, 5815.
(82) Walters, G.; Sargent, E. H. Effect of Rubidium Incorporation on the Structural, Electrical, and Photovoltaic Properties of Methylammonium Lead Iodide-Based Perovskite Solar Cells. *J. Phys. Chem. Lett.* **2018**, *9*, 1018−1027.
(83) Devanathan, R.; Corrales, L. R.; Gao, F.; Weber, W. J. Signal variance in gamma-ray detectorsA review. *Nucl. Instrum. Methods Phys. Res., Sect. A* **2006**, *565*, 637−649.
(84) Park, S. H.; Roy, A.; Beaupre, S.; Cho, S.; Coates, N.; Moon, J. S.; Moses, D.; Leclerc, M.; Lee, K.; Heeger, A. J. Bulk heterojunction solar cells with internal quantum efficiency approaching 100%. *Nat. Photonics* **2009**, *3*, 297.
(85) Wei, H.; Fang, Y.; Mulligan, P.; Chuirazzi, W.; Fang, H.-H.; Wang, C.; Ecker, B. R.; Gao, Y.; Loi, M. A.; Cao, L.; Huang, J. Sensitive X-ray detectors made of methylammonium lead tribromide perovskite single crystals. *Nat. Photonics* **2016**, *10*, 333.
(86) Hou, G.-J.; Wang, D.-L.; Ali, R.; Zhou, Y.-R.; Zhu, Z.-G.; Su, G. $CH_3NH_3PbI_3$/GeSe bilayer heterojunction solar cell with high performance. *Sol. Energy* **2018**, *159*, 142−148.

NOTE ADDED AFTER ASAP PUBLICATION

This paper was published on October 20, 2020, with an incorrect author affiliation. The corrected version was reposted on October 22, 2020.

https://dx.doi.org/10.1021/acsami.0c14595
ACS Appl. Mater. Interfaces 2020, 12, 49636−49647